Check for updates

Imaging spatial variations of optical bandgaps in perovskite solar cells

Boyi Chen,[1] Jun Peng,[1] Heping Shen,[1] The Duong,[1] Daniel Walter,[1] Steve Johnston,[2] Mowafak M. Al-Jassim,[2] Klaus J. Weber,[1] Thomas P. White,[1] Kylie R. Catchpole,[1] Daniel Macdonald,[1*] and Hieu T. Nguyen[1*]

[1]Research School of Engineering, The Australian National University, Canberra, ACT 2601, Australia

[2]National Renewable Energy Laboratory, Golden, CO 80401, USA

[*]Email: hieu.nguyen@anu.edu.au, daniel.macdonald@anu.edu.au

Keywords: perovskite, luminescence, bandgap, photovoltaic, imaging

We develop a fast, non-destructive, camera-based method to capture optical bandgap images of perovskite solar cells (PSCs) with micron-scale spatial resolution. This imaging technique utilizes well-defined and relatively symmetrical band-to-band luminescence spectra emitted from perovskite materials, whose spectral peak locations coincide with absorption thresholds and thus represent their optical bandgaps. We employ the technique to capture relative variations in optical bandgaps across various PSCs, and to resolve optical bandgap inhomogeneity within the same device due to material degradation and impurities. Degradation and impurities were found to both cause optical bandgap shifts inside the materials. Our results are confirmed with micro-photoluminescence spectroscopy scans. The excellent agreement between the two techniques opens opportunities for this imaging concept to become a quantified, high spatial resolution, large-area characterization tool of PSCs. This development continues to strengthen the high value of luminescence imaging for the research and development of this photovoltaic technology.

Author Manuscript

This is the author manuscript accepted for publication and has undergone full peer review but has not been through the copyediting, typesetting, pagination and proofreading process, which may lead to differences between this version and the Version of Record. Please cite this article as doi: 10.1002/aenm.201802790.

This article is protected by copyright. All rights reserved.

1. Introduction

Performance of organic-inorganic metal halide perovskite solar cells (PSCs) has dramatically improved over the past decade. Following the first PSCs reported in 2009 with a photon-to-electricity power conversion efficiency of ~4% [1], optimization of material compositions and device structures has boosted their efficiency to more than 23 % [2]. This new technology has attracted significant attention from researchers and is regarded as one of the most promising candidates for the next-generation photovoltaics (PV).

As one of the most fundamental and critical parameters of perovskite materials, the bandgap energy can affect many of their optical and electrical properties. A common optical-based approach to estimate bandgaps of direct-gap semiconductors are to employ absorption spectroscopy. In this approach, one captures absorption spectra of materials and obtains absorption thresholds from Tauc plots [3]. The Tauc analysis provides a consistent way to compare among materials. However, as mentioned by Green *et al.* [4], these thresholds represent optical bandgaps, not electronic bandgaps, as the Tauc analysis underestimates the presence of excitonic transitions and broadening factors such as temperatures, defect densities and material disorders [4,5]. Alternatively, one can capture the so-called band-to-band luminescence spectra from materials, which are results of radiative recombination between free electrons and holes in the conduction and valence bands, respectively. The peak wavelengths (or energies) of the luminescence spectra have been reported to be close to the absorption thresholds at room temperature by numerous authors [6-10] (also see **Figure S1, Supporting Information**). Thus, the two optical methods can be used to estimate the material optical bandgap although they often underestimate the true electronic bandgap. However,

Author Manuscript

This article is protected by copyright. All rights reserved.

both of these approaches measure the spatially-average optical bandgap over a certain area. Therefore, capturing spatially-resolved optical bandgaps of the entire sample area requires point-by-point mapping in both X and Y directions, and thus it is time consuming and impractical for large-area device imaging or high-throughput production-line environments.

In PV research and manufacturing, luminescence imaging, including both electroluminescence (EL) and photoluminescence (PL), is a mainstream characterization tool for crystalline silicon solar cells [11-17]. This camera-based method can provide fast diagnostics of PV materials and devices with micron-scale spatial resolution. Recently, luminescence imaging has increased in significance for perovskite device and material characterization. Many works have extracted various device parameters of PSCs such as correlations between luminescence intensities and open-circuit voltages [18-20], spatial distributions of nonradiative recombination centers [21,22], series resistances from EL images [23], and lateral inhomogeneities on each sub-cell in monolithic perovskite-silicon tandem structures [24]. It is also a powerful tool for monitoring long-term performance and stability of PSCs [25-27]. Given such a wide range of applications, EL and PL-based imaging could soon become dominant characterization techniques for this promising PV technology due to the rapid progress to scale up PSCs for commercialization purposes [28-30]. Therefore, any more capability added into a standard imaging tool, without sacrificing its advantages, is highly desirable.

Current EL/PL imaging tools typically capture an aggregate luminescence signal from an entire device and disregard the rich information contained in its spectra. Hyperspectral imaging is an alternative approach which compromises between luminescence imaging and spectroscopy. The technique utilizes one physical dimension of a camera chip (X or Y) as a physical dimension on the sample

Author Manuscript

This article is protected by copyright. All rights reserved.

surface (X or Y), and the other physical dimension of the chip as a spectral dimension to provide a luminescence spectrum for each pixel on a sample [31-34]. Thus, one, in principle, can extract an optical bandgap image, which is an image of peak locations of band-to-band luminescence spectra, from the sample using hyperspectral imaging tools. However, to image the whole device, one has to scan the camera (or a sample stage) along one direction of the device. Thus, it requires a much longer measurement time than a standard imaging tool. For example, with a 1024×1024 pixel camera chip, hyperspectral imaging would require 1024 images to have the same spatial resolution as standard luminescence imaging, as one physical dimension of the chip needs to be sacrificed to resolve the spectral information. Another disadvantage of the hyperspectral imaging technique is that, the tool needs to incorporate a spectrograph and a scanning stage and thus it is much more complex than a standard imaging system.

In this work, we develop a camera-based method to image the optical bandgap of an entire PSC with high spatial resolution in a fast and non-destructive manner. First, we explain the underlying principle of our technique. After that, we demonstrate it on various PSCs (negligible hysteresis). The newly-developed technique enables us to resolve variations in optical bandgaps across various devices and optical bandgap non-uniformities of the perovskite film within the same device due to cell degradation and impurities. Our results are confirmed with micro-photoluminescence spectroscopy (μ-PLS) measurements, a well-accepted method to quantify optical bandgaps of direct-gap PV materials [35-37].

Author Manuscript

This article is protected by copyright. All rights reserved.

Author Manuscript

2. Method Description

First, we explain the underlying physics of our imaging concept. Highly-efficient metal halide PSCs have been reported to yield relatively symmetrical band-to-band luminescence spectra at room temperature without any sub-bandgap signal [24,34,38-40]. In order to verify this, we capture luminescence spectra from various perovskite films with different compositions and plot them in **Figure 1**. We observe that these spectra can be reasonably fitted with Gaussian distributions in which the peak location (λ_0) and full-width at half-maximum (*FWHM*) are two fitting parameters. These peak locations (λ_0) match the absorption edges from Tauc plots (**Figure S1**, **Supporting Information**). Also, the PL spectral shapes are not significantly affected by the glass substrates, in particular the peak locations (**Figure S2**, **Supporting Information**). Thus, they can be considered as the optical bandgaps of perovskite materials. We see that λ_0 for the multiple cation perovskite film is at a shorter wavelength (or higher photon energy), consistent with increased transparency to short-wavelength light as desired for tandem applications [37]. In addition, the functional form of the emission spectra (i.e. approximately Gaussian) does not change depending on the peak wavelength of emission. Instead, the spectra are distinguished by the λ_0 and *FWHM* fit parameters, a fact we will exploit to extract the optical bandgap from the intensity of spectrally-filtered intensity images.

This article is protected by copyright. All rights reserved.

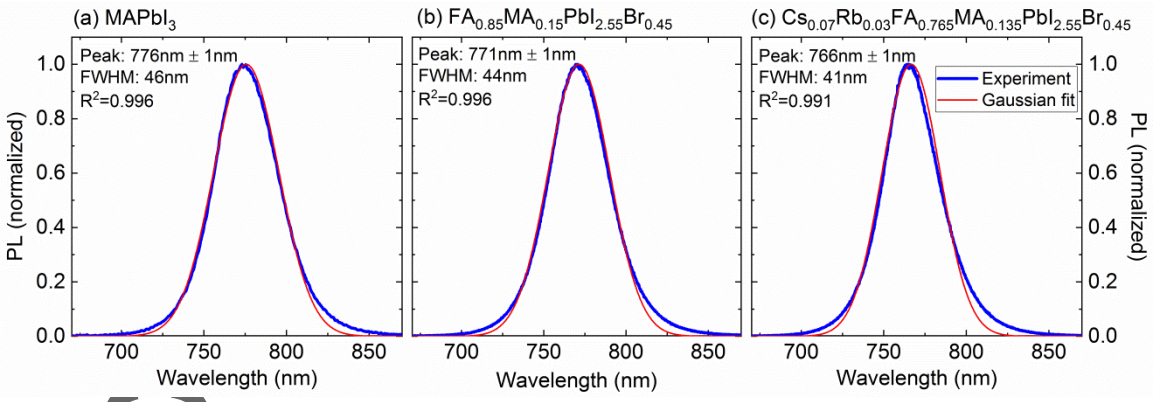

Figure 1: PL spectra of various perovskite films with different compositions and corresponding Gaussian fits. (a) $MAPbI_3$. (b) $FA_{0.85}MA_{0.15}PbI_{2.55}Br_{0.45}$. (c) $Cs_{0.07}Rb_{0.03}FA_{0.765}MA_{0.135}PbI_{2.55}Br_{0.45}$. MA = methylammonium, FA = formamidinium.

In luminescence images, emitted photons pass through various optical components before reaching a detector. The detected intensity in each pixel is a wavelength-dependent integration of the product of the emitted spectrum and optical responses of system components located along the pathway between a sample and the detector. Generally, we have the following relationship between the detected intensity *I* and the emitted spectrum from each pixel on the sample:

$$I = A \times \int Gaussian(\lambda_0, FWHM) \times R_{det}(\lambda) \times T_{objective}(\lambda) \times T_{filters}(\lambda) d\lambda \quad \textbf{(Equation 1)},$$

where *A* is an intensity scaling factor, R_{det} is the spectral response of the detector, $T_{objective}$ is the transmission response of the objective lens used to image the sample, and $T_{filters}$ is the combined transmission response of all optical filters. The latter three parameters (R_{det}, $T_{objective}$, $T_{filters}$) are all wavelength dependent and their values can be determined for a certain imaging system. In addition, *A* typically must be calibrated in order to convert the luminescence intensity into an absolute photon number.

Author Manuscript

This article is protected by copyright. All rights reserved.

With three different optical filters, two intensity ratios:

$$Ratio\ 1 = \frac{I_{\ 1}\ with\ optical\ filter\ 1}{I_{\ 2}\ with\ optical\ filter\ 2} \text{ and } Ratio\ 2 = \frac{I_{\ 1}\ with\ optical\ filter\ 1}{I_{\ 3}\ with\ optical\ filter\ 3}$$

will be fixed for a given imaging system with a certain combination of {λ_0, *FWHM*}. The intensity scaling factor (*A*) is also cancelled out. Thus, we can simulate these two ratios for a range of {λ_0, *FWHM*} and pre-store the data. They serve as a look-up table to extract peak wavelengths (considered to be optical bandgaps) of perovskite materials by experimentally capturing three intensity luminescence images using the three optical filters.

We note that this Gaussian fitting procedure does not necessarily describe all physical properties which contribute to luminescence signals. A luminescence spectrum is a complex combination of many physical phenomena inside materials and devices such as surface morphologies, device structures, material disorders and densities of states, to name a few [41,42]. The main purpose of this technique is to quickly extract peak locations of band-to-band luminescence spectra, and thus optical bandgaps of the material.

In fact, the imaging concept mentioned above can be generalized for other semiconductor materials and devices to extract various spectral parameters, given that no defect luminescence is present. A band-to-band luminescence spectrum emitted from a semiconductor can be described in the form of $I(\lambda) = A \times f(u_1, u_2, \dots, u_N)$ where {u_1, u_2..., u_N} are *N* unknowns and f is an arbitrary function operator describing the spectral shape. **Equation 1** can then be generalized into:

$$I = \int I(\lambda) \times R_{det}(\lambda) \times T_{objective}(\lambda) \times T_{filters}(\lambda) d\lambda \qquad \textbf{(Equation 2)}.$$

Author Manuscript

This article is protected by copyright. All rights reserved.

Therefore, it is possible to extract all unknowns $\{u_1, u_2..., u_N\}$ from the intensity I with enough equations. In this way, it is analogous to solving N unknowns using N equations. A simple way to achieve this is to capture luminescence intensity images with various optical filters having different transmissivities.

3. Results

3.1. Bandgap images of various PSCs

Figure 2 shows an example of two simulated luminescence intensity ratios with three different optical filters. **Figure 2a** is the ratio between 750-nm long-pass (LP) and 775-nm LP filters, and **Figure 2b** is between 750-nm LP and 775-nm short-pass (SP) filters. One very important point in these figures is that the ratios are much more sensitive to peak wavelengths λ_0 than to *FWHMs*. With a fixed *FWHM*, the ratios vary significantly with various λ_0 (illustrated by a vertical dash line in **Figure 2b**). However, with a fixed λ_0, various *FWHMs* may give the same ratio (illustrated by a horizontal dash line in **Figure 2b**). This is due to the symmetrical shape of the Gaussian distribution and valid for a variety of filter combinations (see **Figure S3, Supporting Information**).

Author Manuscript

This article is protected by copyright. All rights reserved.

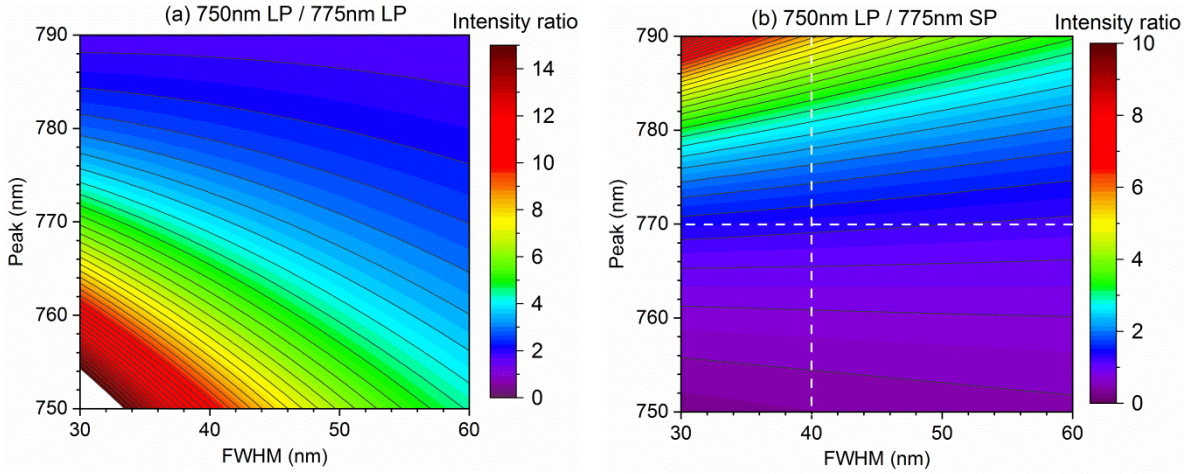

Figure 2: Simulations of luminescence intensity ratios with various combinations of {λ_0, *FWHM*}. (a) 750-nm long-pass filter divided by 775-nm long-pass filter. (b) 750-nm long-pass filter divided by 775-nm short-pass filter.

Figure 3 shows optical bandgap images obtained from our method for various PSCs. **Figure 3a** and **3b** are results for two cells in the same batch whereas **Figure 3c** are for various cells from various batches. For all batches, the same fabrication processes, conditions, transport layers, and composition mixtures were used (see **Experimental Details**). **Figure 3a.1** and **3b.1** are EL intensity images whereas **Figure 3a.2** and **3b.2** are extracted optical bandgap images. We can observe various spots with reduced EL intensities in the solar cells (dark areas in **Figure 3a.1** and **3b.1**). The optical bandgaps of these spots are also shifted (**Figure 3a.2** and **3b.2**). They could be impurities incorporated during the solution preparation or unreacted PbI_2 causing I-rich regions [43,44]. In order to verify these results, we use a μ-PLS system to perform X-Y mapping of the luminescence spectra across the regions indicated by the dashed lines in **Figure 3a.2** and **3b.2** (see **Experimental Details**). This μ-PLS technique provides an entire spectrum for every pixel in the X-Y map, allowing an extraction of an optical bandgap map (i.e. peak position of the spectrum) with micron-scale spatial

Author Manus

This article is protected by copyright. All rights reserved.

resolution. The optical bandgap maps (**Figure 3a.3** and **3b.3**) match with the optical bandgap images (**Figure 3a.2** and **3b.2**) very well, confirming the optical bandgap shifts of the observed spots. A clear advantage of our method, as shown here, is how it can reveal that the optical bandgap between ostensibly equivalent PSC compositions and structures can vary significantly. In the examples of **Figure 3c**, we see that the optical bandgap shifts from approximately 1.63 eV to 1.57 eV. Many authors have demonstrated that small changes in the precursor composition and preparation conditions (e.g., molar ratios, deposition methods, and annealing) can all have dramatic impacts on the properties of the perovskite films, as well as the performance and stability of cells made from the films [45-47]. Therefore, the observed optical bandgap shifts, possibly due to unintentional process inconsistencies, could potentially affect the device performance significantly. Although equivalent information can be obtained from a localized luminescence spectrum measurement, our imaging-based approach can verify that the optical bandgap is uniformly different across the entire cell. The corresponding μ-PLS optical bandgap maps are given in **Supporting Information**, **Figure S4**. By comparison, a localized measurement may be misled by a localized region of optical bandgap variation, as shown in **Figure 3a**. Therefore, it is clear that beyond inhomogeneity in morphology, the composition variation is a significant factor to consider to further improve the reproducibility of PSCs.

Author Manuscript

This article is protected by copyright. All rights reserved.

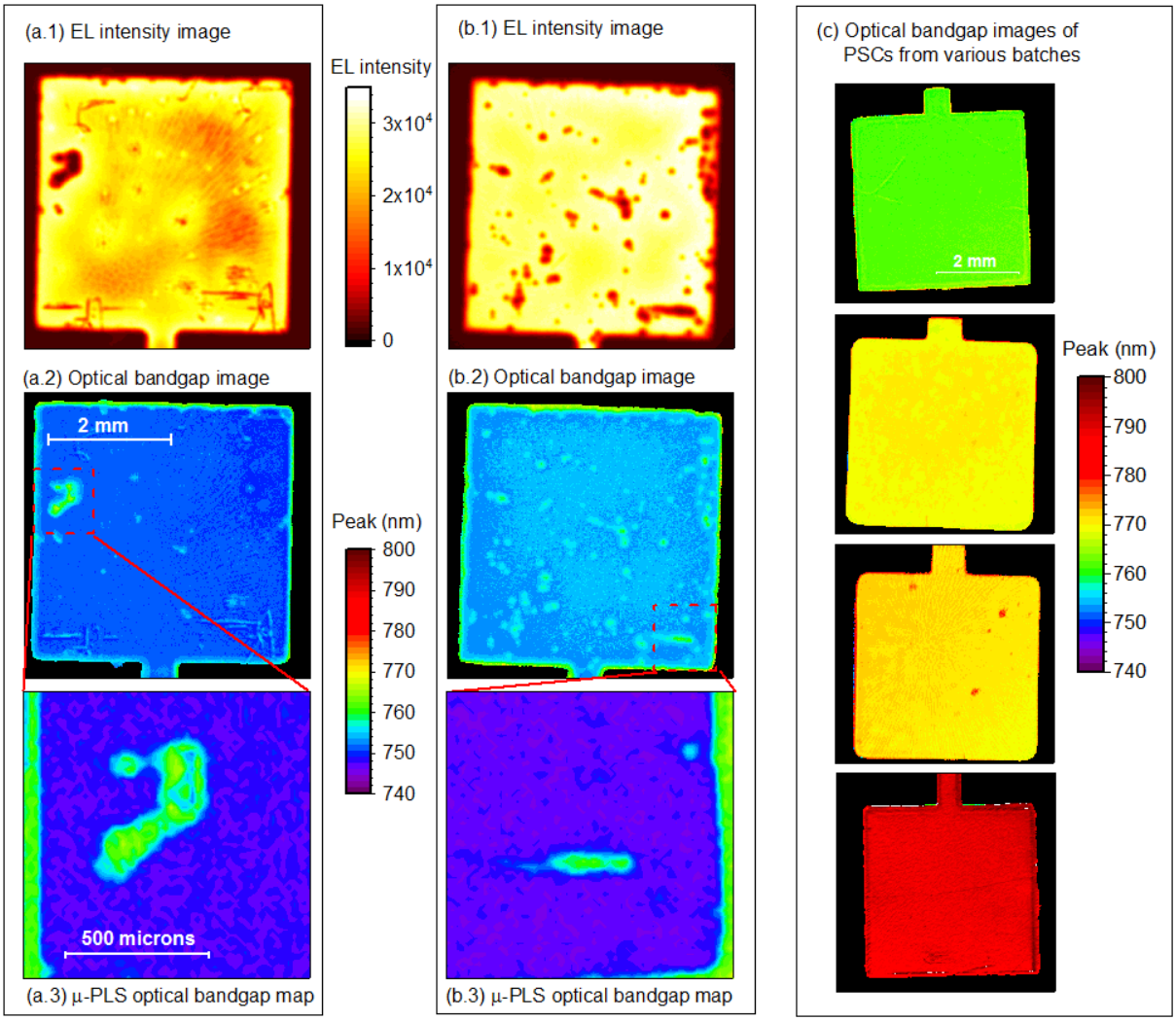

Figure 3: (a.1, b.1) EL intensity images of two PSCs in the same batch. (a.2, b.2) Extracted optical bandgap images from the EL intensity images. (a.3, b.3) Optical bandgap maps extracted from μ-PLS scans, confirming the results from the EL-imaging method. (c) Optical bandgap images for PSCs from various batches, from the top to the bottom: ~1.63 eV (760 nm), ~1.61 eV (770 nm), ~1.60 eV (775 nm), and ~1.58 eV (785 nm). The intended initial composition mixture is $Cs_{0.07}Rb_{0.03}FA_{0.765}MA_{0.135}PbI_{2.55}Br_{0.45}$.

Next, we apply our technique to investigate the implications of PSC instability on the optical bandgap by measuring a PSC degraded after a long period of storage in a nitrogen environment

Author

This article is protected by copyright. All rights reserved.

without humidity control (>2 months). **Figure 4a** and **4b** show EL intensity and extracted optical bandgap images of this solar cell, respectively. As can be clearly seen, the edge region is severely degraded and the perovskite optical bandgap energy decreases around the cell edges. The bandgap non-uniformity is confirmed by the µ-PLS map in **Figure 4c**. A combination of two images (**Figure 4a** and **4b**) allows us to relate the material optical bandgaps to EL intensities, as shown in **Figure 4d**. The degraded signal is strongly correlated with the optical bandgap shift. However, this optical bandgap shift is not obvious until the cell is severely degraded (more than one order of magnitude reduction in EL intensities). This storage-induced optical bandgap shift is consistent with a recent report [48] where the authors also observed a red-shift in PL spectra after they had stored their samples in a humidity-controlled environment for several weeks. They attributed the shift to the incorporation of H_2O molecules in the crystal lattice [48].

In this analysis, we do not aim to investigate the physical and chemical origins of the localized regions of impurity and degradation, nor how to overcome them. Here, our primary purpose is to demonstrate the high value of our newly-developed technique to quickly capture the variation in the optical bandgap, one of the most important parameters of the entire PSC, with very high spatial resolution using a standard luminescence imaging tool. A key concern, however, when considering degraded or non-uniform regions of the cell is whether the luminescence spectra still maintain their quasi-Gaussian shape, which is necessary to ensure an accurate extraction of λ_0 using our method. Using µ-PLS measurements, we confirmed that the localized regions of degradation in **Figure 3a**, **3b** and **4** still exhibited Gaussian-like distributions, with no change in the quality-of-fit of the Gaussian function (see **Figure S5, Supporting Information**). Furthermore, we also did not find any evidence of

Author Manuscript

This article is protected by copyright. All rights reserved.

sub-bandgap luminescence at room temperature. Thus, our method to extract their optical bandgaps is still applicable.

Our method can also provide information on the mechanisms of degradation taking place under various conditions (temperature, voltage, light, storage, etc.) across a broad type of samples, from large-area PSCs to cell precursors. For example, the optical bandgap variation should relate to a change in material composition. However, in **Figure 4d**, the EL intensity reduction does not necessarily correlate to the optical bandgap variation unless the sample is severely degraded. As EL emission can be strongly affected by the current injection (and extraction) efficiency, the initial degradation suggests that the interface between the perovskite layer and the transport layer and/or the transport layers themselves are likely to be degraded before the absorber during the storage. Therefore, combining both luminescence intensity and optical bandgap images could be useful for the study of how the degradation happens (e.g. in the absorber or at interfacial layers).

Author Manuscript

This article is protected by copyright. All rights reserved.

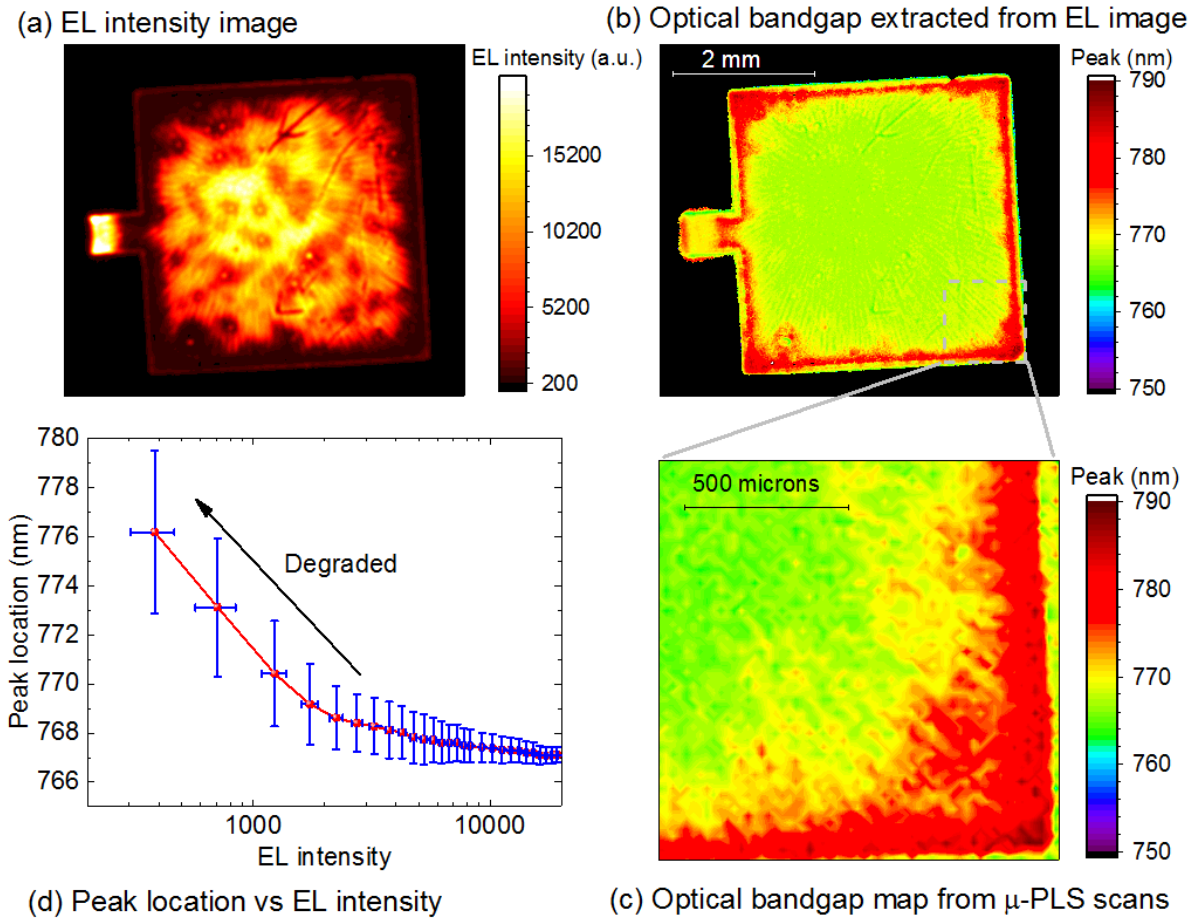

Figure 4: (a) EL intensity image of a degraded perovskite solar cell. (b) Extracted optical bandgap image from the EL intensity image. (c) Optical bandgap map extracted from μ-PLS scans, confirming the results from the EL-imaging method. (d) Peak locations (i.e. optical bandgaps) versus EL intensities.

3.2. Impacts of filters

In this work, we have used a specific selection of short- and long-pass filters. The position of the transmission band edge of these filters was motivated by the sensitivity of our optical bandgap imaging technique to the transmission spectra of the filters. In particular, the fraction of the transmitted spectrum that made up of the tail-ends of the emitted luminescence spectrum was

Author V

This article is protected by copyright. All rights reserved.

found to have a significant impact on the accuracy of the optical bandgap energy. As can be seen across all spectra in **Figure 1** and **5**, the two tails of each spectrum are poorly fit by the Gaussian function (shaded regions of **Figure 5**). In particular, the long-wavelength tail (i.e. low-energy) is always much broader than the Gaussian fit. As mentioned above, a Gaussian function is a relatively simple way to present a spectrum and underestimates various complex phenomena inside the material. Thus, if the filter is not appropriately chosen, the detected spectral part can be dominated by the tails, leading to a significant error in our results.

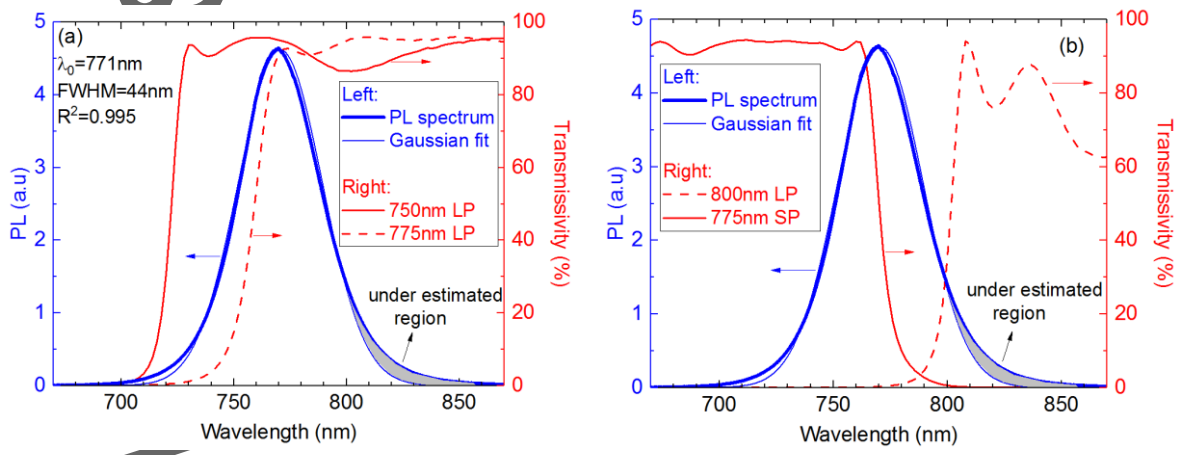

Figure 5: Illustration of impacts of filter choices on the accuracy of our technique. The transmissivity curves of our long-pass and short-pass filters are plotted on the right axis.

In order to illustrate the possible extent of the error from improper filter selection, we illustrate the calculated optical bandgap energy using two combinations of three filters, as required by our method. In **Figure 5a** we plot the transmission spectra of 750-nm LP and 775-nm LP filters. The shaded region at the long-tail of the emission spectra, which represents the total error of the fit, represent ~2% and ~3% of the total integrated signal detected through these filters. In **Figure 5b**, we

Author Manuscript

This article is protected by copyright. All rights reserved.

plot the transmission spectra of two possible choices for the third filter. In the first case, we use a suitable 775-nm SP filter, for which the total error of the detected signal is ~2%. However, if we were to choose an 800-nm LP filter, the under estimated region of our fit would represent roughly 50% of the transmitted signal. To illustrate the impact of this high-error choice of filter, **Figure 6a** and **6b** present the optical bandgap images for the 775-nm SP filter, and the 800-nm LP filter, respectively. The image with the 800-nm LP filter (**Figure 6b**) shows both an unrealistic variation in, and a large error in the absolute magnitude of, the optical bandgap across the sample. Our µ-PLS results confirm that the optical bandgap is uniform (~775 nm) and matches with the image in **Figure 6a**. The key practical implication of this demonstration is that the expected optical bandgap of the material should inform the choice of suitable LP and SP filters. For unknown samples, one needs to use established techniques such as absorption or luminescence spectroscopy to estimate the average optical bandgap first. Indeed, these requirements are the major drawbacks of our technique. In our study, one filter is always either a LP or SP filter having a cut-off wavelength far from the expected optical bandgap. The other two filters are a LP and a SP filter having cut-off wavelengths around the expected optical bandgap. As the FWHMs of perovskite luminescence spectra are ~44 nm (~90 meV), the combination of the three filters should allow resolving optical bandgap variations of ±22 nm (±45 meV) within the expected value, in principle.

Author Manuscript

This article is protected by copyright. All rights reserved.

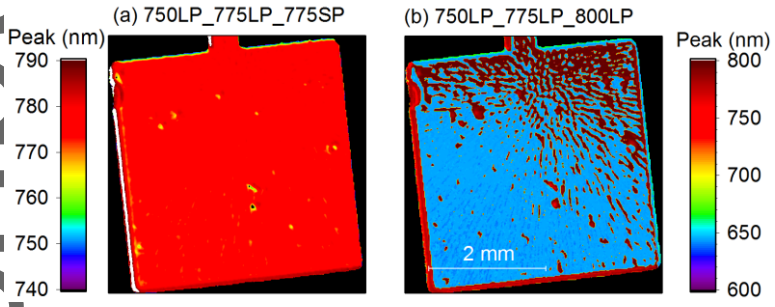

Figure 6: Comparison of extracted optical bandgap images from EL intensity images with various filter combinations.

4. Discussion

A critical assumption in the preceding analysis is that the intensity of the luminescence emission is unchanged between each luminescence image captured with the optical filters. This is because the intensity ratio of the three (or more) images are the key parameter in determining the position of the luminescence spectra peak, λ_0. It is, of course, well understood that perovskites can be inherently unstable materials, subject to reversable or irreversible changes (e.g. through ion migration or material degradation). In the experimental configuration applied in this work, the filters were manually swapped, which introduced a delay of at least 10 seconds between each measurement. Even a reversible change in luminescence emission (i.e. via ion migration) would introduce significant error to the calculations. Therefore, it was essential that we determined that the cell had reached a sufficiently stable operating point before the measurements were taken.

Author Manuscript

This article is protected by copyright. All rights reserved.

The PSCs measured here had very low current-voltage hysteresis when measured using a continuous forward to reverse to forward sweep at 50 mV/s following an open-circuit pre-bias of 30 s. (see **Figure S6**, **Supporting Information**). However, despite low current-voltage hysteresis the photoluminescence emission intensity under open-circuit (**Figure 7b**) took approximately 20s to stabilize. This indicates that the excess carrier density reduces with time following illumination, possibly the result of ion migration influencing recombination rates within the device [49-51]. The PL spectra measured during stabilization and beyond (**Figure 7a**) show no change in peak position (λ_0 = 773 nm). This indicates that the presumed ion migration has no meaningful impact on the location of the optical bandgap, or consequently the perovskite composition.

In addition, one can use either EL or PL imaging to extract optical bandgap images, as both PL and EL emission spectra will be equivalent [34] (**Figure S7**, **Supporting Information)**. PL imaging has the advantage of being contactless, and can be applied to uncontacted perovskite films, or for example films encapsulated with a poly(methyl methacrylate) (PMMA) layer which is known to prevent the film degradation [10,52,53]. EL imaging, on the other hand, requires electrical contact to inject charge carriers into the perovskite layer. We note however, that for the cells investigated, the injected current also changes over time, indicating a change in recombination rates or series resistance (e.g. via contact delamination [25]) during measurements (**Figure 7c**). However, for our purposes, EL imaging provided a direct gauge of the cell stability by allowing us to monitor the injected current over timety, and the optical bandgap measurement was performed once the injected current had stabilized, as indicated in **Figure 7c**.

Author Manuscript

This article is protected by copyright. All rights reserved.

The need for cell stabilization clearly increases the measurement time. However, in industrial applications, a three-camera configuration can capture each image simultaneously, rendering the transient response of the cell irrelevant to the measurement accuracy. This assumes that the luminescence spectrum itself is unchanged during stabilization, which we have verified for the cells investigated here, as shown in **Figure 7a**. Furthermore, increases in cell efficiency and reductions in J-V hysteresis have been correlated with improved stabilization rates [40,54], and we can expect that as PSC performance improves, so too will the stabilization speeds.

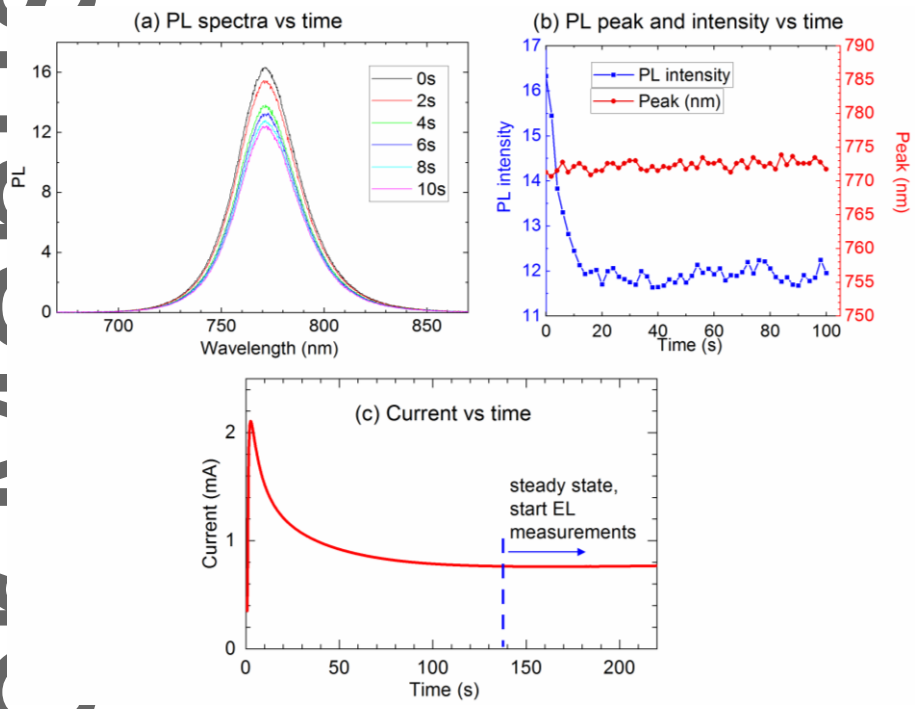

Figure 7: Evolution of PL spectra (a) and (b) spectral peak positions and intensities versus time. (c) Solar cell current versus time, illustrating when EL measurements were performed.

Author Manuscript

This article is protected by copyright. All rights reserved.

5. Conclusion

We have developed a fast, non-destructive, camera-based luminescence method to capture optical bandgap images of perovskite solar cells with high spatial resolution. This new technique utilizes well-defined and relatively symmetrical band-to-band luminescence spectra emitted from perovskite materials, whose spectral peak locations represent their optical bandgaps. We have applied the technique to capture optical bandgap variations across various hysteresis-free perovskite solar cells, and optical bandgap non-uniformities within the same device due to material degradation and impurities. Finally, we have verified our results with micro-photoluminescence spectroscopy scans. The agreement between the two techniques open exciting opportunities for this imaging concept to be a quantified, high spatially resolved, large-area characterization tool of perovskite materials and devices. This could be significant for the study of various degradation mechanisms, morphology homogeneity and reproducibility improvements, or process monitoring on large-area cells and precursors.

6. Experimental Details

Bare perovskite film preparation: $MAPbI_3$ precursor solution contains 1 M equimolar of methylammonium iodide (MAI) and PbI_2 in the mixture of N,N-Dimethylformamide (DMF) and dimethyl sulfoxide (DMSO) (7/3, v/v). The solution was spin-coated on the substrate at 5000 rpm, and chlorobenzene was dropped on the substrate for fast crystallization 10 s after the spin coating commenced. The substrate was then annealed at 100 ^{0}C for 10 mins. $FA_{0.85}MA_{0.15}PbI_{2.55}Br_{0.45}$ precursor solution contains 1.2 M PbI_2, 1.1 M formamidinium iodide (FAI), 0.2 M lead bromide ($PbBr_2$), and 0.2 M methylamine bromide (MABr), in 1 mL anhydrous DMF: DMSO

Manuscript

This article is protected by copyright. All rights reserved.

(8:2, v/v). Quadruple-cation perovskite precursor solution ($Cs_{0.07}Rb_{0.03}FA_{0.765}MA_{0.135}PbI_{2.55}Br_{0.45}$) contains 1.2 M PbI_2, 1.1 M FAI, 0.2 M $PbBr_2$, 0.2 M MABr, 0.091 M CsI, and 0.039 M RbI in 1 mL anhydrous DMF: DMSO (8:2, v/v). The deposition process for each perovskite is the same using two-step spin coating program: first at 2000 rpm with a ramp of 400 rpm s^{-1} for 10 s, and then at 4000 rpm with a ramp of 1000 rpm s^{-1} for 25 s. During the second step, ~100 µl chlorobenzene was poured on the spinning substrates 5 s prior to the end of the program. Substrates were then annealed at 100 ^{0}C for 30 mins.

Perovskite device fabrication: First, ~70 nm In-TiO_x compact layers and ~100 nm mesoporous TiO_2 (30 NRD, Dyesol) layers were sequentially deposited on the pre-cleaned FTO (7Ω/□, Dyesol) substrates according to Ref. [54]. Second, for the ultra-thin PMMA:PCBM [54] passivation layer deposition, 30 µL PMMA:PCBM precursor solution was dropped on the top of the FTO/*c*-In-TiO_x/*m*-TiO_2 substrates and separately deposited by spin-coating at 5000 rpm with a ramp of 5000 rpm s^{-1} for 30 s, then annealed at 100 ^{0}C for 10 min. Then, $Cs_{0.07}Rb_{0.03}FA_{0.765}MA_{0.135}PbI_{2.55}Br_{0.45}$ [40] thin film was deposited by a two-step spin coating program: first at 2000 rpm with a ramp of 200 rpm s^{-1} for 10 s, and then at 4000 rpm with a ramp of 1000 rpm s^{-1} for 20 s. During the second step, around 100 µl Chlorobenzene was poured on the spinning substrates 5 s prior to the end of the program. Substrates were then annealed at 100 ^{0}C for 45 min. Then, Spiro-OMeTAD thin film was deposited via spin coating at 3000 rpm with a ramp of 3000 rpm s^{-1} for 30 s. Finally, ~100 nm gold was deposited through a shadow mask (cell's effective area, 0.16 cm^2). Note that all depositions were conducted in a nitrogen-filled glovebox.

AU

This article is protected by copyright. All rights reserved.

Micro-photoluminescence spectroscopy (μ-PLS): The μ-PLS system employed in this study was a Horiba LabRAM system equipped with confocal optics, a silicon charge-couple-device (CCD) detector, and an automatic X-Y mapping stage. The excitation source was a diode-pumped solid-state (DPSS) 532-nm laser. The excitation light was focused into the sample surface using a 50× objective lens with a numerical aperture of 0.55. The on-sample illumination spot size was ~1 micron and the on-sample power was kept constant at ~20 microwatts. The spectral response of the entire system was determined with a calibrated halogen-tungsten light source. All measurements were performed in a nitrogen gas environment.

Electroluminescence imaging: The solar cells were biased with a supplied voltage of 1.2 V and the current was monitored with a Metrohm Autolab PGSTAT128N potentiostat. Images were captured using a Princeton Instruments Pixis 1024 camera with a Peltier-cooled (-70 °C) silicon CCD detector. The pixel resolution is 14.6 ± 0.1 μm. The cells were kept in a nitrogen gas chamber during the measurements. Transmission responses of all optical filters and objective lenses involved in the measurements were measured using a Perkin Elmer spectrophotometer.

Supporting Information

Supporting Information is available from the Wiley Online Library or from the author.

Acknowledgements

This work has been supported by the Australian Renewable Energy Agency (ARENA) through Research Grant RND017 and the U.S. Department of Energy under Contract No. DE-AC36-08GO28308 with the National Renewable Energy Laboratory (NREL). The authors acknowledge the facilities and technical support from the Australian National Fabrication Facility (ANFF), ACT Node. H.T.N. acknowledges the fellowship support from the Australian Centre for Advanced Photovoltaics (ACAP).

Author Manuscript

This article is protected by copyright. All rights reserved.

Author contributions

H.T.N. conceived the idea, designed the overall experiments, and supervised the project. D.M. co-supervised the project. B.C. performed EL/PL measurements and simulations. J.P., H.S., and T.D. prepared and characterized the perovskite materials and devices. J.P., H.S., T.D., D.W., S.J., M.M.A., K.J.W., T.P.W., K.R.C., and D.M. contributed to the results analysis and interpretation. H.T.N. and B.C. analyzed the data and wrote the manuscript. All authors contributed to the discussion of the results and reviewed the manuscript.

Conflict of Interest

The authors declare no conflict of interest.

Received: ((will be filled in by the editorial staff))
Revised: ((will be filled in by the editorial staff))
Published online: ((will be filled in by the editorial staff))

References

[1] A. Kojima, K. Teshima, Y. Shirai, T. Miyasaka, *J. Am. Chem. Soc.* **2009**, 131, 6050.

[2] NREL's "Best Research-Cell Efficiencies" Chart, version July 17th, 2018.

[3] J. Tauc, R. Grigorovici, A. Vancu, *Physica Status Solidi (b)* **1966**, 15, 627.

[4] M. A. Green, Y. Jiang, A. M. Soufiani, A. Ho-Baillie, *J. Phys. Chem. Lett.* **2015**, 6, 4774.

[5] B. Wenger, P. K. Nayak, X. Wen, S. V. Kesava, N. K. Noel, H. J. Snaith, *Nat. Commun.* **2017,** 8, 590.

[6] K. Wu, A. Bera, C. Ma, Y. Du, Y. Yang, L. Li, T. Wu, Phys. *Chem. Chem. Phys.* **2014**, 16, 22476.

Author Manuscript

This article is protected by copyright. All rights reserved.

[7] S. D. Stranks, V. M. Burlakov, T. Leijtens, J. M. Ball, A. Goriely, H. J. Snaith, *Physical Review Applied* **2014**, 2, 034007.

[8] R. L. Milot, G. E. Eperon, H. J. Snaith, M. B. Johnston, L. M. Herz, *Adv. Funct. Mater.* **2015**, 25, 6218.

[9] T. Wang, B. Daiber, J. M. Frost, S. A. Mann, E. C. Garnett, A. Walsh, B. Ehrler, *Energy Environ. Sci.* **2017**, 10, 509.

[10] S.-H. Turren-Cruz, A. Hagfeldt, M. Saliba, *Science* **2018**, 362, 449.

[11] T. Trupke, R. A. Bardos, M. C. Schubert, W. Warta, *Appl. Phys. Lett.* **2006**, 89, 044107.

[12] J. A. Giesecke, M. The, M. Kasemann, W. Warta, *Progress in Photovoltaics: Research and Applications* **2009**, 17, 217.

[13] J. Haunschild, M. Glatthaar, M. Demant, J. Nievendick, M. Motzko, S. Rein, E. R. Weber, *Solar Energy Materials & Solar Cells* **2010**, 94, 2007.

[14] A. Y. Liu, D. Walter, S. P. Phang, D. Macdonald, *IEEE Journal of Photovoltaics* **2012**, 2, 479.

[15] H. C. Sio, S. P. Phang, D. Macdonald, *Solar RRL* **2017**, 1, 1600014.

[16] Y. Zhu, M.K. Juhl, T. Trupke, Z. Hameiri, *IEEE Journal of Photovoltaics* **2017**, 7, 1087.

[17] R. Bhoopathy, O. Kunz, M. Juhl, T. Trupke, Z. Hameiri, *Prog. Photovolt. Res. Appl.* **2018**, 26, 69.

[18] W. Tress, N. Marinova, O. Inganäs, M. K. Nazeeruddin, S. M. Zakeeruddin, M. Graetzel, *Adv. Energy Mater.* **2015**, 5, 1400812.

[19] Z. Hameiri, A. Mahboubi Soufiani, M. K. Juhl, L. Jiang, F. Huang, Y.-B. Cheng, H. Kampwerth, J. W. Weber, M. A. Green, T. Trupke, *Prog. Photovolt. Res. Appl.* **2015**, 23, 1697.

[20] M. Stolterfoht, C. M. Wolff, J. A. Márquez, S. Zhang, C. J. Hages, D. Rothhardt, S. Albrecht, P. L. Burn, P. Meredith, T. Unold, D. Neher, *Nat. Energy* **2018**, 3, 847.

[21] S. Mastroianni, F. D. Heinz, J.-H. Im, W. Veurman, M. Padilla, M. C. Schubert, U. Würfel, M. Grätzel, N.-G. Park, A. Hinsch, *Nanoscale* **2015**, 7, 19653.

[22] A. M. Soufiani, M. J. Y. Tayebjee, S. Meyer, A. Ho-Baillie, J. S. Yun, R. W. MacQueen, L. Spiccia, M. A. Green, Z. Hameiri, *J. Appl. Phys.* **2016**, 120, 35702.

[23] D. Walter, Y. Wu, T. Duong, J. Peng, L. Jiang, K. C. Fong, K. Weber, *Adv. Energy Mater.***2018**, 2, 1701522.

Author Manuscript

This article is protected by copyright. All rights reserved.

[24] L. E. Mundt, F. D. Heinz, S. Albrecht, M. Mundus, M. Saliba, J. P. Correa-Baena, E. H. Anaraki, L. Korte, M. Gratzel, A. Hagfeldt, B. Rech, M. C. Schubert, S. W. Glunz, *IEEE J. Photovoltaics* **2017**, 7, 1081.

[25] A. M. Soufiani, Z. Hameiri, S. Meyer, S. Lim, M. J. Y. Tayebjee, J. S. Yun, A. H.-Baillie, G. J. Conibeer, L. Spiccia, M. A. Green, *Adv. Energy Mater.* **2017**, 7, 1602111.

[26] H. Shen, Y. Wu, J. Peng, T. Duong, X. Fu, C. Barugkin, T. P. White, K. Weber, K. R. Catchpole, *ACS Appl. Mater. Interfaces* **2017**, 9, 5974.

[27] A. M. Soufiani, J. Kim, A. H.-Baillie, M.Green, Z. Hameiri, *Adv. Energy Mater.* **2018**, 8, 1702256.

[28] T. M. Schmidt, T. T. Larsen-Olsen, J. E. Carlé, D. Angmo, F. C. Krebs, *Adv. Energy Mater.***2015**, 5, 1500569.

[29] S. T. Williams, A. Rajagopal, C.-C. Chueh, A. K.-Y. Jen, *J. Phys. Chem. Lett.* **2016**, 7, 811.

[30] A. Priyadarshi, L. J. Haur, P. Murray, D. Fu, S. Kulkarni, G. Xing, T. C. Sum, N. Mathews, S. G. Mhaisalkar, *Energy Environ. Sci.* **2016**, 9, 3687.

[31] E. Olsen and A. S. Flø, *Appl. Phys. Lett.* **2011**, 99, 011903.

[32] M. P. Peloso, J. Sern Lew, T. Trupke, M. Peters, R. Utama, A. G. Aberle, *Appl. Phys. Lett.* **2011**, 99, 221915.

[33] A. Delamarre, L. Lombez, J.-F. Guillemoles, *Journal of Photonics for Energy* **2012**, 2, 027004.

[34] G. E.-Hajje, C. Momblona, L. G.-Escrig, J. Avila, T. Guillemot, J.-F. Guillemoles, M. Sessolo, H. J. Bolink, L. Lombez, *Energy Environ. Sci.* **2016**, 9, 2286.

[35] V. D'Innocenzo, A. R. S. Kandada, M. D. Bastiani, M. Gandini, A. Petrozza, *J. Am. Chem. Soc.* **2014**, 136, 17730.

[36] L. Protesescu, S. Yakunin, M. I. Bodnarchuk, F. Krieg, R. Caputo, C. H. Hendon, R. X. Yang, A. Walsh, M. V. Kovalenko, *Nano Lett.* **2015**, 15, 3692.

[37] T. Duong, Y. Wu, H. Shen, J. Peng, X. Fu, D.l Jacobs, E.-C. Wang, T. C. Kho, K. C. Fong, M. Stocks, E. Franklin, A. Blakers, N. Zin, K. McIntosh, W. Li, Y.-B. Cheng, T. P. White, K. Weber, K. Catchpole, *Adv. Energy Mater.* **2017**, 7, 1700228.

[38] X. Fu, D. A. Jacobs, F. J. Beck, T. Duong, H. Shen, K. R. Catchpole, T. P. White, *Phys. Chem. Chem. Phys.* **2016**, 18, 22557.

Author Manuscript

This article is protected by copyright. All rights reserved.

[39] T. Duong, H. K. Mulmudi, Y. Wu, X. Fu, H. Shen, J. Peng, N. Wu, H. T. Nguyen, D. Macdonald, M. Lockrey, T. P. White, K. Weber, K. Catchpole, *ACS Applied Materials & Interfaces* **2017**, 9, 26859.

[40] J. Peng, Y. Wu, W. Ye, D. A. Jacobs, H. Shen, X. Fu, Y. Wan, N. Wu, C. Barugkin, H. T. Nguyen, D. Zhong, J. Li, T. Lu, Y. Liu, M. N. Lockrey, K. J. Weber, K. R. Catchpole, T. P. White, *Energy Environ. Sci.* **2017**, 10, 1792.

[41] P. Würfel, *J. Phys. C: Solid State Phys.* **1982**, 15, 3967.

[42] G. D. Gilliland, *Materials Science and Engineering* **1997**, R18, 99.

[43] E. T. Hoke, D. J. Slotcavage, Emma R. Dohner, Andrea R. Bowring, H. I. Karunadasa, M. D. McGehee, *Chem. Sci.* **2015**, 6, 613.

[44] T. Duong, H. K. Mulmudi, Y. Wu, X. Fu, H. Shen, J. Peng, N. Wu, H. T. Nguyen, D. Macdonald, M. Lockrey, T. P. White, K. Weber, K. Catchpole, *ACS Applied Materials & Interfaces* **2017**, 9, 26859.

[45] J. Emara, T. Schnier , N. Pourdavoud , T. Riedl, K. Meerholz, S. Olthof, Adv. Mater. **2016**, 28, 553.

[46] K. A. Bush, K. Frohna, R. Prasanna, R. E. Beal, T. Leijtens, S. A. Swifter, and M. D. McGehee, *ACS Energy Lett.* **2018**, 3, 428.

[47] P. Fassl, V. Lami, A. Bausch, Z. Wang, M. T. Klug, H. J. Snaith, Y. Vaynzof, Energy & Environmental Science 2018. DOI: 10.1039/c8ee01136b

[48] R. Segovia, G. Qu, M. Peng, X. Sun, H. Shi, B. Gao, *Nanoscale Research Letters* **2018**, 13, 79.

[49] Y. Yuan , J. Chae , Y. Shao , Q. Wang , Z. Xiao, A. Centrone , J. Huang, *Adv. Energy Mater.* **2015**, 5, 1500615.

[50] G. Richardson, S. E. J. O'Kane, R. G. Niemann, T. A. Peltola, J. M. Foster, P. J. Cameron, A. B. Walker, *Energy Environ. Sci.* **2016**, 9, 1476.

[51] D. Walter, A. Fell, Y. Wu, T. Duong, C. Barugkin, N. Wu, T. White, K. Weber, *J. Phys. Chem. C* **2018**, 122, 11270.

[52] Z. Chu, M. Yang, P. Schulz, D. Wu, X. Ma, E. Seifert, L. Sun, X. Li, K. Zhu, K. Lai, *Nature Communications* **2017**, 8, 2230.

Author Manuscript

This article is protected by copyright. All rights reserved.

[53] J. Peng, J. I. Khan, W. Liu, E. Ugur, T. Duong, Y. Wu, H. Shen, K. Wang, H. Dang, E. Aydin, X. Yang, Y. Wan, K. J. Weber, K. R. Catchpole, F. Laquai, S. D. Wolf, T. P. White, *Advanced Energy Materials* **2018**, 8, 1801208.

[54] J. Peng, T. Duong, X. Zhou, H. Shen, Y. Wu, H. K. Mulmudi, Y. Wan, D. Zhong, J. Li, T. Tsuzuki, K. J. Weber, K. R. Catchpole, T. P. White, *Advanced Energy Materials* **2017**, 7, 1601768.

Author Manuscript

This article is protected by copyright. All rights reserved.

Short Summary for

Imaging spatial variations of optical bandgaps in perovskite solar cells

Boyi Chen,[1] Jun Peng,[1] Heping Shen,[1] The Duong,[1] Daniel Walter,[1] Steve Johnston,[2] Mowafak M. Al-Jassim,[2] Klaus J. Weber,[1] Thomas P. White,[1] Kylie R. Catchpole,[1] Daniel Macdonald,[1*] and Hieu T. Nguyen[1*]

[1]Research School of Engineering, The Australian National University, Canberra, ACT 2601, Australia

[2]National Renewable Energy Laboratory, Golden, CO 80401, USA

[*]Email: hieu.nguyen@anu.edu.au, daniel.macdonald@anu.edu.au

Keywords: perovskite, luminescence, bandgap, photovoltaic, imaging

We develop a fast, non-destructive, camera-based method to capture optical bandgap images of perovskite solar cells with micron-scale spatial resolution. This technique allows us to probe relative variations in optical bandgaps across various solar cells, and to resolve bandgap inhomogeneity within the same device due to material degradation and impurities. The results are independently confirmed with other optical-based techniques.

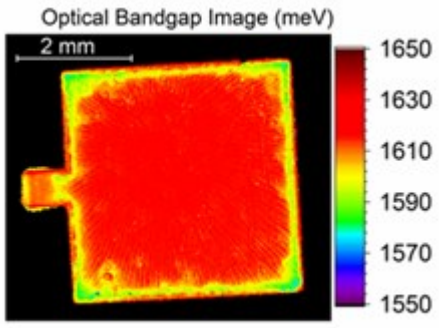

Author Manuscript

This article is protected by copyright. All rights reserved.